LAWRENCE
LIVERMORE
NATIONAL
LABORATORY

LLNL-PROC-645202

Time-resolved x-ray diffraction across water-ices VI/VII transformations using dynamic-DAC

J. Y. Chen, M. Kim, C. Yoo, W. J. Evans

October 24, 2013

2013 Joint APS-SCCM/AIRAPT Conference
Seattle, WA, United States
July 7, 2013 through July 12, 2013

Disclaimer

Time-resolved x-ray diffraction across water-ices VI/VII transformations using *dynamic*-DAC

Jing-Yin Chen[1]*, Minseob Kim[2], Choong-Shik Yoo[2], William Evans[1]
[1]CMMD, Physical & Life Science Directorate, LLNL, Livermore, CA 94551
[2]Institute for Shock Physics, Department of Chemistry, Washington State University, Pullman, WA 99164

E-mail: chen72@llnl.gov

Abstract. We present recent time-resolved x-ray diffraction data obtained across the solidification of water to ice VI and VII at different compression rates. The structural evolution of ice VI to ice-VII, however, occurs rather coarsely. The diffraction data shows an anisotropic compression behaviour of ice VI; that is, the c-axis is more compressible than the a-axis at the same compression rate. Nevertheless, the present equations of state of both ice VI and ice VII obtained under dynamic loadings agree well with those previously obtained under static conditions. Hence, the present study demonstrates the time-resolved x-ray diffraction coupled with *dynamic*-DAC is a good way to investigate the detailed structural response of materials over a wide range of well-controlled compression rates. Finally, we found the evidence for X-ray induced chemical reaction on water and ice VI, presumably hampering the formation of amorphous ice.

1. Introduction

Abundant in nature, water is a major constituent of planets and living organisms. The phase diagram of water, as Fig. 1 exhibits a large number of polymorphs with great diversity in crystalline structure, chemical bonding, and collective interactions [1-3]. The bond angles and topology of relatively weak hydrogen bonds (with respect to covalent O-H bonds) are subject to large distortions, which, in turn, lead to proton and structural disorders and a myriad of phases—both stable and metastable ones (including amorphous). In addition to the fifteen known solid phases of H_2O, there are many metastable phases. These include several metastable phases of ice IV near the melt line [4] and metastable ice VII in the stability field of ice VI [5], high- and low-density amorphous (HDA and LDA) at low temperatures [6-10], and high- and low-density water (HDW and LDW) [11]. Furthermore, liquid water under dynamic conditions is observed beyond the equilibrium phase boundaries. Therefore, the stability limit conjecture of liquid water [2], shown as the green curve, is estimated from the homogeneous nucleation temperatures of the super-cooled liquid. Recently, HDA [12] ice is reported at room temperature under rapid compression, forming from metastable ice VII in the stability field of ice VI. This is in addition to a whole series of intermediate structures arising from amorphization, dipole ordering transitions, and symmetrization of hydrogen bonding [6,13]. The strength of OH-bonds varies in these metastable structures, as does the transition dynamics not well understood.

* To whom any correspondence should be addressed.

Recent advances of *dynamic*-DAC [5,12,14-16] enable the studies of metastable/intermediate states controlled by kinetics. For example, dynamic pressure-induced dendrites have been observed with highly unusual four-fold symmetry. In addition, metastable ice VII was observed in the stability field of ice VI, arising from the structural similarity between ice VII and super-compressed water and thereby a lower interfacial energy of ice VII than ice VI. These results clearly demonstrated that *d*-DAC is indeed a powerful method to study transition dynamics of solids over a wide range of well-controlled pressures and compression rates.

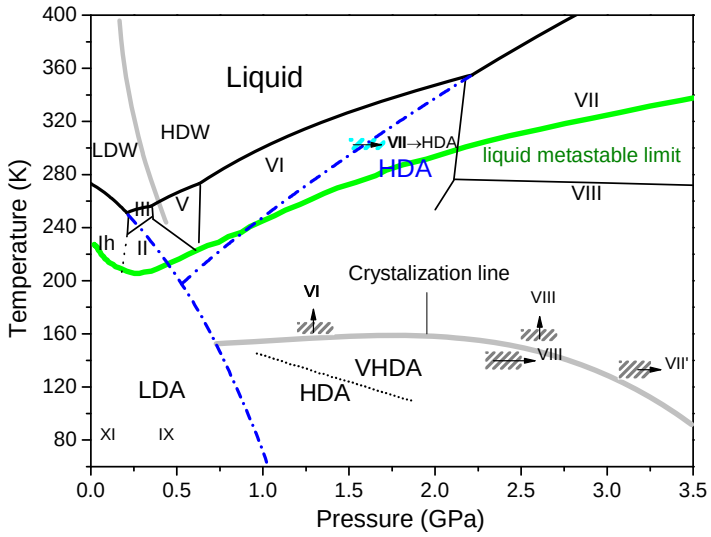

Figure 1. The phase diagram of H_2O showing a wide range of metastable and disordered phases of water and ice. The present data signifies the appearance of metastable ice VII (hatched in baby blue) in the stability field of ice VI at room temperature – well before the equilibrium transition pressure. The blue dashed-dotted curves are the extrapolated melting lines of ice Ih and ice VII. The grey lines show the phase boundary of LDW and HDW [11] and the boundary of crystalline ices and amorphous ices [6]. The green curve is the calculated liquid metastable limit [2].

Recently, HDA was found to form from metastable ice VII in the stability field of ice VI, which was attributed to be due to the structural instability of the parent phase, ice VII. Yet, the detailed structural information of metastable ice VII and its pressure-induced amorphization are not known. Therefore, the present study is to obtain the structural evolution across the solidification of super-compressed water to ice VI and ice VII and understand the structure and structural instability of metastable ice VII, using time-resolved x-ray diffraction coupled with *d*-DAC.

2. Experiments

A small drop of pure distilled water (< 10 nl) was loaded through a stainless steel micro-syringe needle into a small (0.08-0.13 mm) hole on a pre-indented stainless steel gasket mounted between two opposed diamond anvils with 0.3 or 0.5 mm flats, together with a few small ruby chips for pressure calibrations.

Time-resolved diffraction experiments were carried out using monochromatic synchrotron x-rays at 25.7 keV (or 0.48262 Å in wavelength) at the P02 Hard X-ray Diffraction Beamline at PETRA III at DESY. The x-ray beam was highly focused to ~2 (Horizontal) x 7 (Vertical) μm at the sample. A 2-dimesional pixel array x-ray detector (PILATUS 1M or Perkin Elmer) was used, together with a set of electronics for time synchronization and operation of dynamic-DAC including a piezoactuator power amplifier, a function generator, a delay generator, and a digital oscilloscope. High quality polycrystalline CeO_2 standard is used for the calibration of the image plate. The exposure time is set to be 10 s for a reasonable level of signal and resolution in this study.

The present *d*-DAC [14] utilizes three piezo-electric actuators (Piezo Jenna, model PAHL 18/20) to modulate the pressure of a conventional DAC. The peak pressure (P), pressure modulation (ΔP), compression rate ($\Delta P/\Delta t$), and load frequencies (f) of *d*-DAC are precisely controlled by adjusting the waveform of the electric input signal to the piezo-actuators using a function generator and a power amplifier. A digital delay generator is used to synchronously operate all associated instruments including a *d*-DAC, a 2-D x-ray image plate detector, and an oscilloscope. Figure 2 shows a typical oscilloscope record, displaying the trigger (the red curve), modulation (the dark blue curve) and feedback signals from the 2-D image plate (the grey curve). The high voltage of the feedback indicates the detector is on for exposure, whereas the low voltage represents the data is read out to the buffer memory or a PC. The time T_0 (T=0) is when the modulation starts. The timing of each frame is then derived from the feedback of 2-D image plate and T_0. Two types of pressure modulation, square and trapezoid waves, are utilized across the liquid-solid transition. The sample pressure was measured by Ruby luminescence before and after the dynamic loading. Based on the previous study [17], the amorphous ice is suspended when water has impurities. In order to catch the diffraction pattern of HDA, no other materials are used as the pressure indicator. The pressures of samples during dynamic loadings are calculated from the third-order Birch-Murnaghan (BM) equation of state (EOS) for ice VI [19] and ice VII [18].

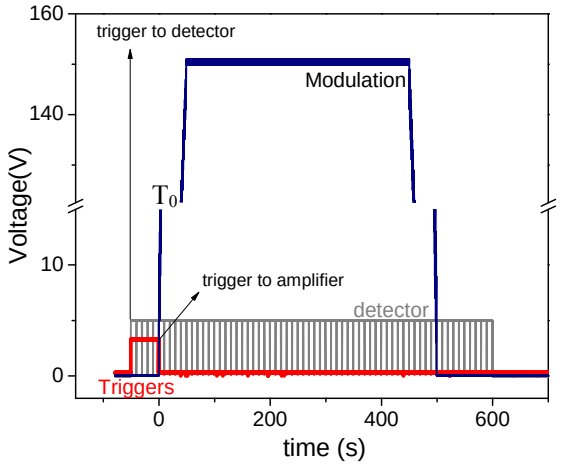

Figure 2. A typical digital oscilloscope record of time-resolved x-ray measurements, showing the trigger (red line) for the 2D x-ray detector and the piezo-actuator amplifier, the feedback from the x-ray detector (grey line), and the actuator modulation (dark blue). The high voltage indicates the detector is on for signal exposure and the low voltage means the data is read out.

All the x-ray diffraction patterns are read by using Fit2D and analyzed by Jade (MDI, Jade 9) to index the diffraction pattern and determine the lattice parameters of ice VI and ice VII. There are nine successful sets of measurements reported in this study.

3. Results and discussions

The metastable ice VII has been observed from super-compressed water at rapid compressions in the stability field of ice VI [5,12]. In addition, the pressure-induced amorphization of metastable ice VII at room temperature, HDA, is observed by high-speed microphotography and time-resolved Raman, resulted from the structural instability of the ice VII [12]. Here, we report the time-resolved x-ray diffraction data probing the structural evolution associated with the solidification of water to ice VI and VII.

(A) Water-iceVI-iceVII transition under dynamic loading

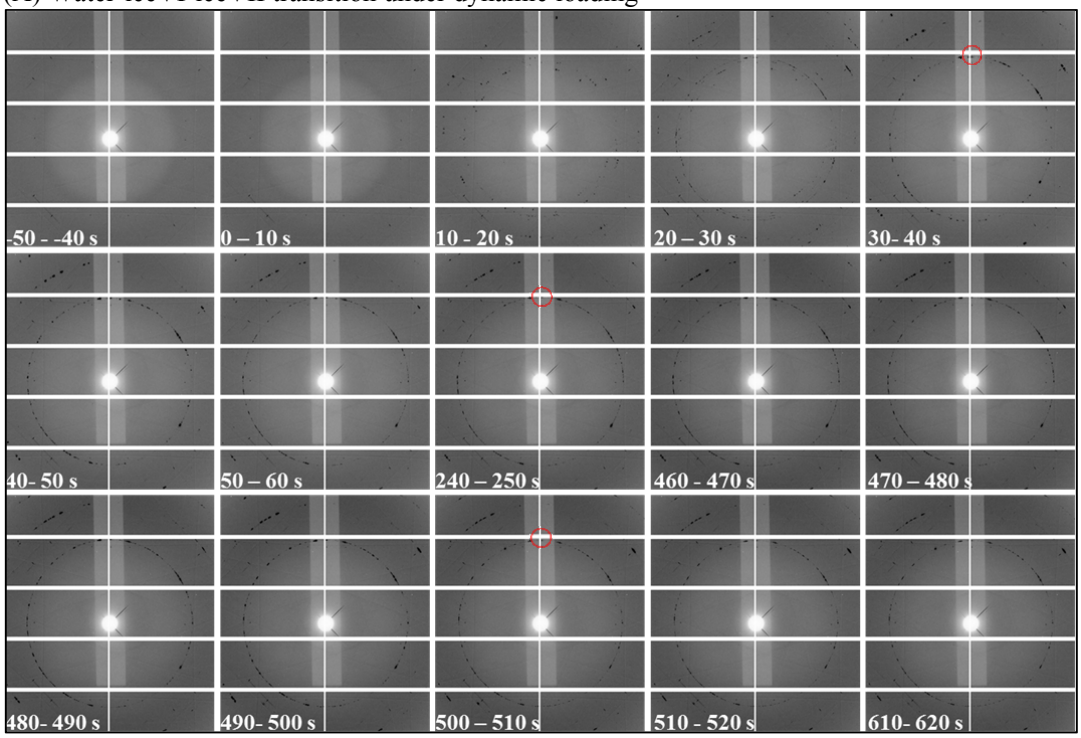

(B) The enlarged x-ray diffraction images of 10-20s, 20-30s, 30-40s, 40-50s, and 50-60s

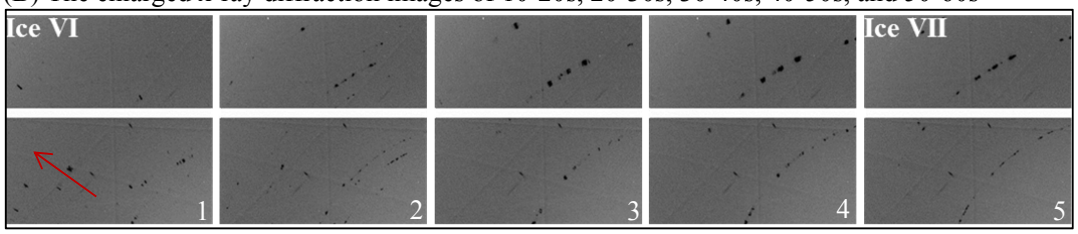

Figure 3. (A) Representative time-resolved x-ray diffraction images of the sample during one dynamic loading. Water solidifies to ice VI and ice VII during compression. The modulation and the timing of this dynamic loading are shown in Fig. 2. The time noted in each image represents the exposure time. T=0 (T_0) is defined as the time when the modulation starts. (B) The enlarged x-ray diffraction images of 10-20s, 20-30s, 30-40s, 40-50s, and 50-60s among (A).

3.1. Water-ice VI-ice VII transitions and water-ice VI transition

A series of time-resolved x-ray diffraction patterns with 10 s exposure time under dynamic loading are illustrated in Fig. 3. The pressure modulation for this representative dynamic loading is illustrated in Fig. 2. The pressure ramping initiates at T_0, and reaches the maximum at T=50s. The pressure will hold at maximum for 450 s and start to decrease linearly at T= 450-500s. As planned, pressure starts to increase at T_0 and the pressure reach the peak pressure at 50 s. At T=0-10s, sample is still in liquid phase, water start to solidify at T=10-20s. In Fig. 3, liquid water is evident by its weak diffuse ring before the dynamic loadings. Note that the diffused signal of water is too weak to study the freezing mechanism of H_2O. The diffraction pattern of 10-20s is identified as ice VI, a tetragonal structure (*$P4_2/nmc$*). More diffraction peaks develop at 20-30s, suggesting a phase transition between 10-20 and 30-40s. The diffraction pattern of 30-40s is identified as ice VII, a body centered cubic structure (bcc, *Pn3m*). The pressure is increasing between T=30 and T=50s, because the bcc (110) diffraction peak shifts outward to a smaller unit cell. As expected, the diffraction patterns between T=50 and T= 450 are almost identical, because the pressures are the same. From T=450 to 500s, the pressure starts to decrease. The (110) diffraction peak shifts inward, to a larger unit cell.

Figure 3(B) shows the enlarged diffraction pattern of a selected area. The diffraction spots in Fig3(B)-1 diffused along the radial direction, showing liquid water transforms into ice-VI, while the pressure increases continuously during the exposure time of 10 s. In Fig.3(B)-2, the diffraction peaks of ice VII appear. In addition, the sizes of diffraction spots are much more localized than those in Fig.3(B)-1 or -3, implying that the pressure remains unchanged during which ice-VI and ice-VII coexist. Based on the pressure modulation and the diffused diffraction spots of ice VII, the pressure increases again until it reaches the maximum at T~50s.

Figure 4 plots the time-resolved diffraction pattern obtained across the water-ice VI-ice VII transition and water-ice VI transition as a function of time and 2θ. The calculated diffraction patterns of ice VI at 1.0 GPa (blue bars) and ice VII at 1.7 GPa (black bars) are shown for comparison. The bar colour intensity is correlated to the calculated diffraction peak intensity, dark blue-baby blue: stronger-weaker. The red curves show the modulations. The diffraction peak intensities are shown in grey scale. In other words, the darker is the stronger. The onset transition times for water-to-ice VI and ice-VI-to-ice VII can be determined in Fig. 4(L). The pressure follows the modulation, except a little delay during the decompression. Water solidifies into ice VI. The diffraction peaks of ice VI are weak, yet they are sufficient to refine the lattice parameters. Ice VII grows when the pressure increases. Based on the response of ice VII and the reported Birch-Murnaghan EOS for ice VII [18], the compression rate is estimated to be 0.13±0.008 GPa/s. The unit cell parameters of ice VII decrease with the increase of pressure. During decompression, the unit cell parameters of ice VII expand. There may be a tiny delay between the modulation and the sample response, because of the time taking for mechanical coupling. The final pressure estimated from ice VII after the dynamic loading is ~4.4 GPa.

In the water-ice VI transition, liquid water (P_i ~ 0.3 GPa from Ruby) transforms into ice VI. The unit cell parameters of ice VI continuously decrease, corresponding to the increase of pressure. The peak pressure, 1.43±0.06 GPa at this dynamic loading is calculated from ice VI, and the compression rate is ~ 0.0105±0.0005 GPa/s. The unit cell of ice VI expands during decompression. The final pressure at this dynamic loading is ~ 0.9±0.15 GPa. During the decompression, the discontinuous appearance of ice VI diffraction peaks in the 2-D time-2Θ plot of water-ice VI transition is possibly because ice VI forms a single crystal as shown in Fig.6(A) and x-ray focus located around the boundary.

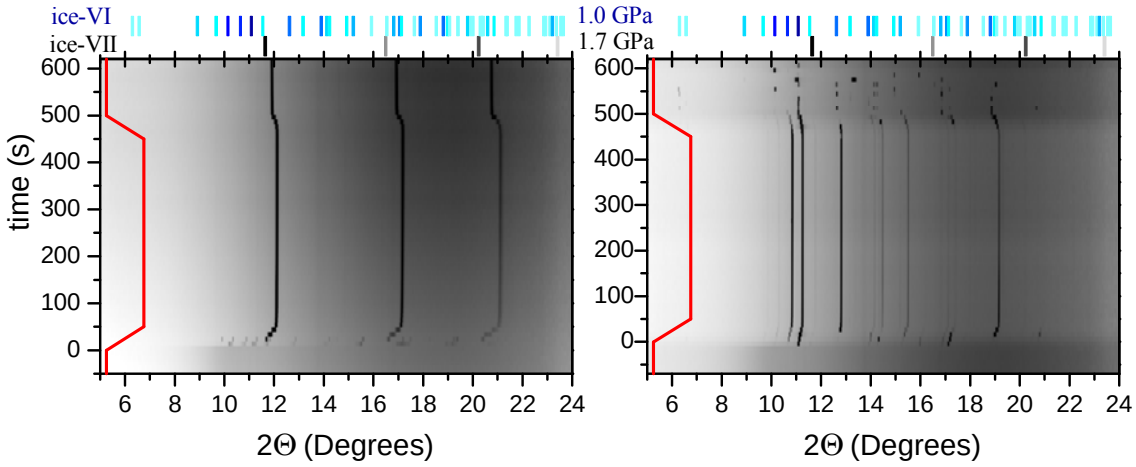

Figure 4. (Left) 2-D time-2Θ plot of the water-ice-VI-ice VII transition. (Right) 2-D time-2Θ plot of the water-ice VI transition. (Upper) the calculated diffraction patterns of ice VI (blue) and ice VII (black). The intensities of diffraction peaks are shown in grey scale. The colour intensity of bar is correlated to the intensity of the ideal diffraction peak. The red curves show the modulations.

3.2. Lattice parameters of ice VI and ice VII

Figure 5(A) plots the lattice parameters of ice VI and ice VII obtained from the diffraction patterns. Note that the dynamic response of the lattice parameters follows the pressure modulation. In the group of trapezoid modulation (solid symbols), a linear response of ice VI lattice parameters to the pressure change is observed at longer ramping time (~50s, on the right of Fig. 5(A)), resulting in the compression rate of 0.01-0.1 GPa/s. At shorter ramping time (~10s, on the left of Fig.5(A)), the 10s-resolution is too long to resolve the evolution of ice VI lattice parameters. In the group of square modulation (open symbols), no lattice parameter during the transition is observed, indicating the water-ice VI transition is really fast with appropriate driving force. The diamond symbols are the data obtained during the water-ice VI-ice VII transition. Note that the c-axis of ice VI has a slightly larger change than the a-axis at the same compression rate. In fact, this is in a good agreement with the reported axial moduli [19], K_a(1.25-225 GPa) = 70.5 (7) GPa and K_c(1.25-2.25 GPa) = 56.2 (5) GPa.

Figure 5(B) illustrates the densities of ice as a function of pressure. As mentioned above, the pressure of ice is determined by the measured lattice parameters and the third-order BM equation of state. The EOS parameters of ice VII [18] are the ambient volume V_0=12.3(±0.2) cm^3/mol, the isothermal bulk modulus at room temperature K_o=23.9 (±0.7) GPa and the pressure derivative of the isothermal bulk modulus K' = 4.2 (± 0.5). In this study, one set of ice VII in pure water are observed at its steady field. Another set of ice VII in "reacted" water is observed at the pressure slightly below the equilibrium phase boundary ~ 2.2 GPa. Regarding the pressure of ice VI, the polynomial fit of the data [19] is used to determine the pressure, because most BM EOS of ice VI are obtained at low temperature. In this study, the densities of ice VI and VII behave as expected. Here, we demonstrate the time-resolved x-ray diffraction technique at a moderate or slow compression rate is a good approach to obtain EOS at very fine pressure increment. So far, the sensitivity in pressure from various pressure markers is low, especially at low pressure range.

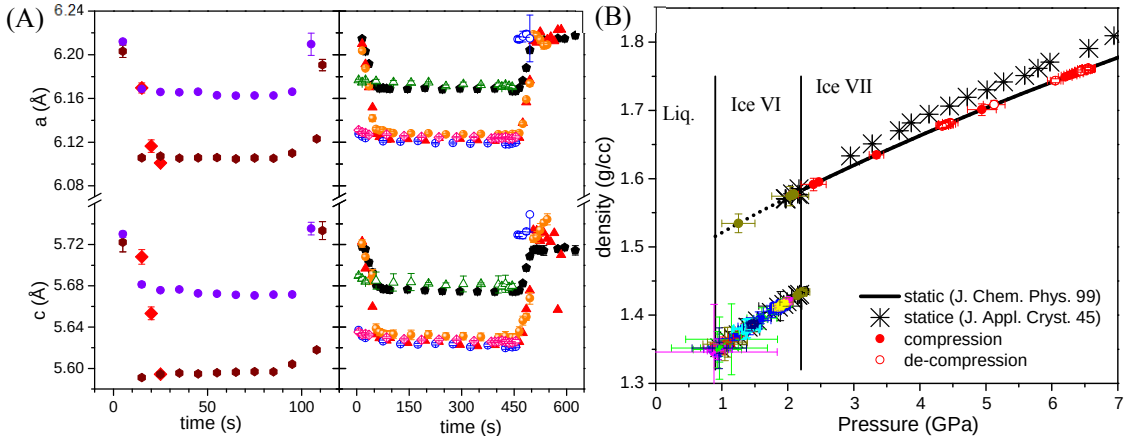

Figure 5. (A) The lattice parameters of ice VI as a function of time at two different time frames. Different symbols are the data from different runs. The closed symbols are the data with trapezoid-wave modulation, and the opens are those with square-wave modulation. (B) Densities of ices plotted as a function of pressure. The circles are the data from the present study. The black curve is calculated from the BM equation and the dotted portion is the extrapolation of the BM equation. The asterisks are the static data recently reported by Fortes et al. The vertical bars illustrate the equilibrium phase boundaries.

3.3. X-ray induced chemical reaction of water

X-ray induced chemical reaction on water is observed in this study, as shown in Fig. 6(B). X-ray induced dissociation of H_2O into O_2-H_2 alloy at high pressure (>2.6 GPa) was reported previously [20]. However, no bobbles, indicating H_2 or O_2, or clatherates are observed in this study. Only the black burning spot is observed, implying the radiation damage. Only water diffuse ring is observed, taken at the burning spot. Based on the previous study [17], the amorphous ice would be suspended when water has some impurity. This is likely the reason for the absence of amorphous ice at higher compression rates. An alternate explanation is the diffraction intensity of amorphous ices or intermediate ice VII is too weak or appear at a very short duration (in μs time scale) for x-ray diffraction. In future, time-resolved x-ray diffraction technique coupled with in-suit high-speed microphotography or time-resolved Raman would be used to address the problem.

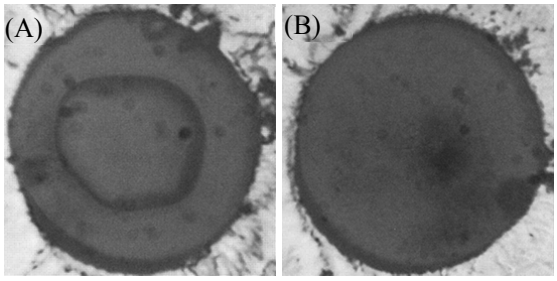

Figure 6. (A) A single crystal of ice VI at ~0.9 GPa. (B) Liquid water at ~0.6 GPa. The black area shows the evidence of the x-ray induced chemical reaction of water.

4. Conclusions

We presented the time-resolved x-ray data across the water-ice VI- ice VII transition and the water-ice VI transition at different compression rates. The structural evolution of ice VI-ice-VII is observed coarsely. It shows that the c-axis of ice VI is more compressible than a at the same compression rate. The present EOS of ice VI and ice VII and the phase boundary under dynamic loadings agree well

with those obtained previously under static conditions. Finally, the possibility of x-ray induced chemical reaction or decomposition should be taken into account for the future diffraction studies.

Acknowledgments
The X-ray studies were performed at the light source Petra III at DESY, a member of the Helmholtz Association (HGF). We would like to thank H.P. Lierrmann and the beamline staffs for assistance in using beam line ECB P02. The work at LLNL was performed under the auspices of the U.S. Department of Energy in part under contract W-7405-Eng-48 and in part under Contract DE-AC52-07NA27344 and supported by the Laboratory Directed Research and Development Program at LLNL under project tracking code 11-ERD-046. The work at WSU has been performed in support of NSF-DMR (Grant No. 1203834), DTRA (HDTRA1-12-01-0020), and Deep Carbon Observatory – Extreme Physics and Chemistry.

References

[1] Hemley RJ, Jephcoat AP, Mao HK, Zha CS, Finger LW, and Cox DE 1987 *Nature* **330** 737
[2] Soper AK 2002 *Science* **297** 1288
[3] Nelmes RJ, Loveday JS, Strassle T, Bull CL, Guthrie M, Hamel G, and Klotz S 2006 *Nat. Phys.* **2** 414
[4] Chou IM, Blank JG, Goncharov AF, Mao H-K, and Hemley RJ 1998 *Science* **281** 809
[5] Lee GW, Evans WJ, and Yoo C-S 2006 *Phys. Rev. B* **74** 134112
[6] Mishima O, Calvert LD, and Whalley E 1984 *Nature* **310** 393; 1985 *Nature* **314** 76
[7] Klotz S, Hamel G, Loveday JS, Nelmes RJ, Guthrie M, and Soper AK 2002 *Phys. Rev. Lett.* **89** 285502
[8] Tse JS, Klug DD, Tulk CA, Swainson I, Svensson EC, Loong CK, Shpakov V, Belosludov VR, Belosludov RV, and Kawazoe Y *Nature* **400** 647
[9] Finney JL, Bowron DT, Soper AK, Loerting T, Mayer E, and Hallbrucker A 2002 *Phys. Rev. Lett.* **89** 205503
[10] Yoshimura Y, Mao H-k, and Hemley RJ 2006 *Chem Phys Lett* **420** 503
[11] Saitta AM and Datchi F 2003 *Phys. Rev. E* **67** 020201
[12] Chen J-Y and Yoo C-S 2011 *Proc. Natl. Acad. Sci. USA* **108** 7685
[13] Knight C, Singer SJ, Kuo J-L, Hirsch TK, Ojamae L, and Klein ML 2006 *Phys. Rev. E* **73** 056113
[14] Evans WJ, Yoo C-S, Lee GW, Cynn H, Lipp MJ, and Visbeck K 2007 *Rev. Sci. Instrum.* **78** 073904
[15] Lee GW, Evans WJ, and Yoo C-S 2007 *Proc. Natl. Acad. Sci. USA* **104** 9178
[16] Chen J-Y and Yoo C-S 2011 *MRS Proc.* **1262**-W04-03
[17] Chen J-Y and Yoo C-S 2012 *J. Phys.:Conf. Ser.* **377** 012109
[18] Fei Y, Mao HK and Hemley RJ 1999 *J. Chem. Phys.* **99** 5369
[19] Fortes AD, Wood IG, Tucker MG, and Marshall WG 2012 *J. Appl. Cryst.* **45** 523.
[20] Mao W, Mao HK, Meng Y, Eng PJ, Hu MY, Chow P, Cai YQ, Shu J, and Hemley RJ 2006 *Science* **314** 636.